A New Drag Relation for Aerodynamically Rough Flow over the Ocean

EDGAR L ANDREAS

NorthWest Research Associates, Inc., Lebanon, New Hampshire

LARRY MAHRT

NorthWest Research Associates, Inc., Corvallis, Oregon

DEAN VICKERS

College of Earth, Ocean, and Atmospheric Sciences, Oregon State University, Corvallis, Oregon

(Manuscript received 21 November 2011, in final form 6 March 2012)

ABSTRACT

From almost 7000 near-surface eddy-covariance flux measurements over the sea, the authors deduce a new air–sea drag relation for aerodynamically rough flow:

$$u_* = 0.0583U_{N10} - 0.243.$$

Here u_* is the measured friction velocity, and U_{N10} is the neutral-stability wind speed at a reference height of 10 m. This relation is fitted to U_{N10} values between 9 and 24 m s^{-1}. A drag relation formulated as u_* versus U_{N10} has several advantages over one formulated in terms of $C_{DN10} = (u_*/U_{N10})^2$. First, the multiplicative coefficient on U_{N10} has smaller experimental uncertainty than do determinations of C_{DN10}. Second, scatterplots of u_* versus U_{N10} are not ill posed when U_{N10} is small, as plots of C_{DN10} are; u_*–U_{N10} plots presented here suggest aerodynamically smooth scaling for small U_{N10}. Third, this relation depends only weakly on Monin–Obukhov similarity theory and, consequently, reduces the confounding effects of artificial correlation. Finally, with its negative intercept, the linear relation produces a C_{DN10} function that naturally rolls off at high wind speed and asymptotically approaches a constant value of 3.40×10^{-3}. Hurricane modelers and the air–sea interaction community have been trying to rationalize such behavior in the drag coefficient for at least 15 years. This paper suggests that this rolloff in C_{DN10} results simply from known processes that influence wind–wave coupling.

1. Introduction

Turbulence research in the atmosphere has built on the groundwork laid by fluid mechanics research in the laboratory. But, atmospheric research may also have suffered by assuming too much similarity with laboratory fluid mechanics. As an example, we consider here drag parameterizations at the air–sea interface.

In fluid mechanics texts, most discussions of fluid motion start with the Bernoulli equation (e.g., Batchelor 1970, p. 158; Faber 1995, p. 46):

$$P + \frac{1}{2}\rho U^2 + \rho g z = \text{const.} \tag{1.1}$$

Here P is the fluid pressure, ρ is the fluid density, U is the flow speed, g is the acceleration of gravity, and z is the height above some arbitrary reference level. This equation essentially states that the energy per unit volume is constant along a streamline in a fluid flow.

We can change this constant, however, by placing an obstacle in the flow—a sphere, for example. The total drag on such an obstacle is generally expressed as

$$D = \frac{1}{2}\rho A C_D U^2, \tag{1.2}$$

where A is the frontal area of the obstacle and C_D is its drag coefficient. In the context of (1.1), D/A can be

---

Corresponding author address: Dr. Edgar L Andreas, NorthWest Research Associates, Inc., 25 Eagle Ridge, Lebanon, NH 03766-1900.
E-mail: eandreas@nwra.com

DOI: 10.1175/JAS-D-11-0312.1

thought of as the change in the constant along a streamline that results from frictional losses to the obstacle; the ½ in (1.2) emphasizes the concept that the drag is a change in kinetic energy per unit volume in the fluid. Because energy can be changed only by adding or subtracting momentum, D/A can also be thought of as a momentum flux.

When the problem turned to understanding the coupling between air and sea, early oceanographers and atmospheric scientists parameterized the wind's drag on the sea surface as in (1.2) (e.g., Sverdrup et al. 1942 479–480, 489–491; Francis 1954; Neumann 1956; Wilson 1960; Roll 1965, p. 152; Neumann and Pierson 1966, 208–210, p. 414):

$$\tau = \rho_a C_{Dr} U_r^2. \tag{1.3}$$

Here τ is the drag per unit area of sea surface (also called the surface stress or the momentum flux), ρ_a is the air density, U_r is the wind speed at some reference height r above the sea, and C_{Dr} is the dimensionless drag coefficient appropriate for r. Although the ½ appeared in some early atmospheric versions of (1.3) (e.g., Sutton 1953, p. 232; von Arx 1967, p. 113) to emphasize its derivation from (1.2), modern version are like (1.3), with the ½ absorbed into C_{Dr}.

With the advent of Monin–Obukhov similarity theory, C_{Dr} became a theoretical—not just empirical—coefficient (e.g., Garratt 1992, 52–55):

$$C_{Dr} = \left[\frac{k}{\ln(r/z_0) - \psi_m(r/L)}\right]^2. \tag{1.4}$$

In this, k (=0.40) is the von Kármán constant; z_0, the roughness length; and ψ_m, an empirical function of the stratification parameter L, the Obukhov length.

Equation (1.4) actually derives through (1.3) from the similarity equation for the wind speed profile in the atmospheric surface layer:

$$U(z) = \frac{u_*}{k}[\ln(z/z_0) - \psi_m(z/L)], \tag{1.5}$$

where z is the height above the surface and u_* is the friction velocity such that

$$\tau \equiv \rho_a u_*^2. \tag{1.6}$$

In (1.5), we see that z_0 is the artificial height at which the wind speed is zero and is presumably a fundamental aerodynamic property of the surface (e.g., Wieringa 1993). Hence, z_0 and C_{Dr} imply the same information.

To emphasize this point and to make comparing measurements of C_{Dr} more meaningful, we usually eliminate the stability dependence in (1.4) and choose 10 m as the standard reference height. Then (1.4) becomes an expression for the neutral-stability, 10-m drag coefficient:

$$C_{DN10} = \left[\frac{k}{\ln(10/z_0)}\right]^2, \tag{1.7}$$

where z_0 is expressed in meters. Likewise, we often plot C_{DN10} versus the neutral-stability wind speed at 10 m, which derives from (1.5) with the stability term ignored:

$$U_{N10} \equiv \frac{u_*}{k}\ln(10/z_0). \tag{1.8}$$

Equations (1.7) and (1.8) also provide the useful result

$$C_{DN10} = \left(\frac{u_*}{U_{N10}}\right)^2. \tag{1.9}$$

Over 50 years of research to develop a unified parameterization for C_{DN10} has, however, not narrowed the range of reported C_{DN10} values or satisfactorily explained that range. Reviews repeatedly show plots of widely spread C_{DN10} values at any given wind speed (e.g., Kraus 1968; Garratt 1977; Blanc 1985; Geernaert 1990; Banner et al. 1999; Toba et al. 2001; Drennan et al. 2005). It has long been suspected that C_{DN10} responds to other variables than just wind speed, including to sea state; see Jones and Toba (2001) for a review. Ignoring these dependencies was presumed to explain the scatter.

We have some other ideas, however, on why C_{DN10} has been so hard to pin down. First, consider the fundamental uncertainty in C_{DN10} as computed from (1.9). Measurements of u_* over the sea have a minimum uncertainty of about ±10%. [See, for instance, Fairall et al. (1996, Table 1) for typical uncertainties.] When u_* is small, this uncertainty can approach ±100%. Although U_r may be measured at sea on a ship, from a tower or buoy, or from an aircraft with an uncertainty of, say, ±5%, obtaining U_{N10} necessitates a stability correction involving L. Because L requires u_*^3 and measurements of the surface heat fluxes, it is probably uncertain by at least ±30%. Hence, the minimum uncertainty in C_{DN10} (i.e., if we assume that U_{N10} has the same uncertainty as U_r) is ±30%. Other phenomena that are presumed to affect C_{DN10}—such as sea state, swell, and the relative wind direction between wind and waves—likely make contributions smaller than this in moderate and high winds (cf. Janssen 1997); these effects are thus hidden in the uncertainty of the basic measurements.

In addition to these fundamental considerations of uncertainty, in stable stratification, the magnitude of ψ_m in (1.4) and (1.5) can become comparable to $\ln(z/z_0)$.

Hence, in light winds, C_{Dr} can become unrealistically small and is dominated by the uncertainty in L. At the same time, U_{N10} can also become very small—and, at times, negative [see (2.1) below]. Clearly C_{DN10} is problematic in such conditions.

Recently, Foreman and Emeis (2010) focused on yet another problem with C_{DN10} by suggesting that the definition of the drag coefficient [which has its roots in (1.2)] is fundamentally flawed. Namely, we could reasonably infer from (1.9) that u_* is proportional to U_{N10} with a proportionality constant of $C_{DN10}^{1/2}$. When Foreman and Emeis plotted roughly a thousand points from the literature as u_* versus U_{N10}, however, they obtained

$$u_* = aU_{N10} + b \tag{1.10}$$

for $U_{N10} \geq 8\ \mathrm{m\ s^{-1}}$ (presumably aerodynamically rough flow). In (1.10), u_* and U_{N10} are in meters per second, $a = 0.051$, and $b = -0.14\ \mathrm{m\ s^{-1}}$. Equation (1.10) shows that u_* is linearly related to U_{N10} but is not proportional to it.

This absence of proportionality is interesting because (1.10) then implies

$$C_{DN10} = \left(\frac{u_*}{U_{N10}}\right)^2 = a^2\left(1 + \frac{b}{aU_{N10}}\right)^2. \tag{1.11}$$

That is, instead of increasing linearly with U_{N10}, as in most formulations of C_{DN10} (e.g., Garratt 1977; Smith 1980; Geernaert 1990; Smith et al. 1992), here C_{DN10} is more complex. Moreover, because b is negative, C_{DN10} rises, rolls off, and asymptotes to a^2 at high wind speed.

The hurricane community has been searching for behavior like this in C_{DN10} since Emanuel (1995) reported that hurricane models could not produce storms with enough intensity if their drag parameterization was simply an extrapolation of results from moderate wind speeds, which had C_{DN10} increasing linearly with U_{N10}, without bounds. Modern hurricane and ocean mixed-layer models, on the other hand, have had some success in predicting storm intensity and ocean response by limiting the value of C_{DN10} in high winds (Jarosz et al. 2007; Moon et al. 2007; Sanford et al. 2007; Chiang et al. 2011).

Equation (1.10) has features aligned with our own philosophy of air–sea interaction: 1) The experimental coefficient a has only half the experimental uncertainty of C_{DN10} and is, thus, more reliably measured; 2) a plot of u_* versus U_{N10} does not have pathological behavior when U_{N10} is near zero, as do plots of C_{DN10}; 3) (1.10) minimizes reliance on Monin–Obukhov similarity theory and thereby suffers little from the fictitious correlation typical of these types of analyses (e.g., Mahrt et al. 2003; Klipp and Mahrt 2004; Grachev et al. 2007a,b; Andreas 2011b); and 4) (1.11) produces a natural limit to C_{DN10}.

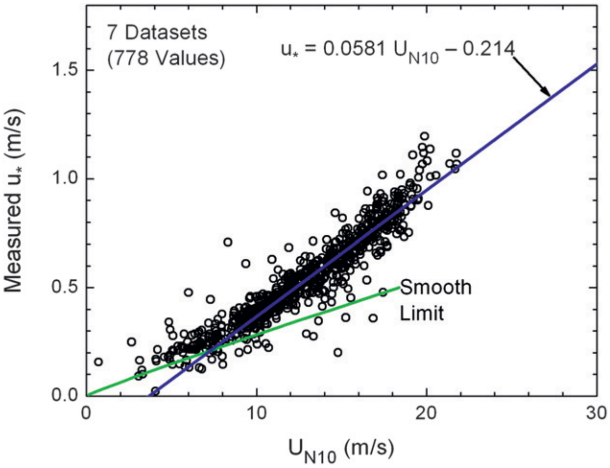

FIG. 1. Our "original" dataset plotted as u_* vs U_{N10} (see Table 1). The blue line, (1.12), is the best fit through the data that represent aerodynamically rough flow, $U_{N10} \geq 9\ \mathrm{m\ s^{-1}}$. The green line shows the relationship between u_* and U_{N10} in aerodynamically smooth flow, (4.1). The plot does not include the CBLAST hurricane data listed in Table 1.

Because of these merits in (1.10), after reading Foreman and Emeis (2010), we quickly plotted u_* versus U_{N10} for data that we had on hand. Figure 1 shows that our results corroborate those of Foreman and Emeis. We find

$$u_* = 0.0581U_{N10} - 0.214 \tag{1.12}$$

for data in the aerodynamically rough flow regime, $U_{N10} \geq 9\ \mathrm{m\ s^{-1}}$; the correlation coefficient of these data is 0.929. We will elaborate on this figure later; but, for now, it showed enough promise for us to commit to a full study of the drag parameterization that Foreman and Emeis suggested.

As such, we add over 6000 more values measured by low-flying aircraft in winds up to 27 m s^{-1} to the 778 points shown in Fig. 1. This aircraft set also shows a straight-line relation between u_* and U_{N10} in the aerodynamically rough regime, and the fitting coefficients are not statistically different from those in (1.12).

Both datasets also suggest that u_* follows the prediction for aerodynamically smooth flow for low U_{N10}. Consequently, we devise a continuous drag relation for all U_{N10} by smoothly combining this aerodynamically smooth regime with (1.10) for the aerodynamically rough regime.

On extrapolating this relation to hurricane-strength winds, we find that it predicts the rolloff in C_{DN10} that hurricane models seem to require. Moreover, the

TABLE 1. Our original datasets come from tabulations in the cited references or were provided by the cited authors. The ''Number of runs'' gives the number of u_*–U_{N10} pairs in the dataset. The cited wind speed range is for U_{N10}.

Dataset	Number of runs	Range in wind speed (m s^{-1})	Platform/location	Reference
CBLAST-hurricane	48	16.5–29.0	NOAA P3, Hurricanes Fabian and Isabel	French et al. (2007)
FASTEX	264	0.7–20.2	R/V *Knorr*, transect across the North Atlantic	Persson et al. (2005)
GFDex	109	4.9–21.8	FAAM BAE 146 aircraft, Irminger Sea and Denmark Strait	Petersen and Renfrew (2009)
HEXOS	173	5.6–18.3	Meetpost Noordwijk platform, North Sea	DeCosmo (1991)
Janssen	100	7.2–20.2	Meetpost Noordwijk platform, North Sea	Janssen (1997)
RASEX	80	4.1–16.2	Tower, Vindeby in Denmark–Langeland–Lolland area	Johnson et al. (1998)
SOWEX	25	5.1–19.5	CSIRO F27 aircraft, off southwest coast of Tasmania	Banner et al. (1999)
SWADE	126	3.5–14.2	*Frederick G. Creed*, off coast of Virginia and North Carolina	Donelan et al. (1997)

straight-line behavior of u_* with U_{N10}—even in high winds—and the rolloff in C_{DN10} are compatible with theoretical models by Moon et al. (2007) and Mueller and Veron (2009) that compute the air–sea drag as resulting from just skin friction and the form drag from flow separation over the waves. In other words, our analysis suggests that there is no need to invoke exotic processes, such as sea spray loading or the disintegration of the air–sea interface, to explain the roll off in C_{DN10} with increasing wind speed. Wind–wave coupling suffices.

2. Datasets

Table 1 summarizes the data with which we made our first test of the Foreman and Emeis (2010) approach (i.e., our Fig. 1). We will refer to this as the ''original'' dataset. Most of these sets are available as tabulations in the cited references. We obtained the Fronts and Atlantic Storm Track Experiment (FASTEX) and Greenland Flow Distortion Experiment (GFDex) data, however, as electronic files from the scientists referenced for these sets.

We did not include the Coupled Boundary Layers Air–Sea Transfer (CBLAST) hurricane dataset mentioned in Table 1 in this analysis because these data are not consistent with our other data: The u_* values tend to be low, as we will show later. We suspect that this bias resulted because these aircraft data were obtained at flight levels that were never below 70 m, were as high as 383 m, and had a median level of 193 m, while the depth of the boundary layer for these flights during Hurricanes Fabian and Isabel was 350–550 m (Zhang et al. 2009). That is, because the stress is known to decrease with height through the boundary layer (e.g., Caughey et al. 1979; Nicholls and Readings 1979; Zhang et al. 2009; Wyngaard 2010, 244–247, 286–287), the measured flight-level stress was less than the surface stress. Although French et al. (2007) tried to correct for this flux divergence, their reported values of u_* remain low.

Table 2 summarizes a second set of data that we use in this study. Because all of these data come from low-flying aircraft, we will refer to this as our ''aircraft'' dataset.

Four different aircraft collected these data: the National Oceanic and Atmospheric Administration's Long-EZ, the C-130 and Electra from the National Center for Atmospheric Research (NCAR), and the Twin Otter from the Naval Postgraduate School's Center for Interdisciplinary Remotely Piloted Aircraft Studies (CIRPAS) (Khelif et al. 2005).

To measure the turbulent wind vector required for computing the momentum flux, the Twin Otter, C-130, and Electra used five-port radomes on the nose of the aircraft. Each port had a pressure sensor that sampled at 20–25 Hz; Lenschow (1986) describes the principles of obtaining the wind vector from aircraft pressure measurements. Each of these three aircraft used the Global Positioning System (GPS) to correct the aircraft's inertial navigation system to find true ground speed (Khelif et al. 1999).

The Long-EZ used the Best Atmospheric Turbulence Probe (BAT) for measuring the wind vector (Crawford and Dobosy 1992; Garman et al. 2006). This is a baseball-bat-shaped device with nine pressure ports in its thicker end; it protruded from the Long-EZ into the undisturbed free stream ahead of the aircraft. A pressure sensor in each port sampled at 50 Hz; again, the aircraft's inertial navigation system was corrected with GPS positioning to obtain the true wind vector with respect to the ground.

Regardless of aircraft, each flux value in the aircraft set is the average over a 4-km flight segment that we processed ourselves from the raw data. We use the flight-level momentum flux as $\rho_a u_*^2$: that is, we made no adjustments for height because the aircraft were always below 50 m.

TABLE 2. Our "aircraft" dataset consists of 4-km flight segments that we processed ourselves; see Mahrt et al. (2012) for additional details. "Number of runs" here is the number of such 4-km legs. The "Altitude range" gives the aircraft flight level; the wind speed noted is the range of measured wind speeds at those levels. The cited references give more details on the measurements.

Dataset	Number of runs	Altitude range (m)	Range in wind speed (m s^{-1})	Aircraft/location	Reference
CARMA4	650	27–40	0.5–18.1	CIRPAS Twin Otter, off coast of southern California	
CBLAST-weak	740	1–16	1.4–9.3	Long-EZ, Martha's Vineyard, MA	Edson et al. (2007)
GOTEX	859	24–49	2.3–27.1	NCAR C-130, Gulf of Tehuantepec	Romero and Melville (2010)
Monterey	654	26–39	2.2–18.0	CIRPAS Twin Otter, off Monterey, CA	Mahrt and Khelif (2010)
POST	189	22–40	2.6–13.9	CIRPAS Twin Otter, off Monterey, CA	
RED	373	23–49	1.4–19.9	CIRPAS Twin Otter, east of Oahu, Hawaii	Anderson et al. (2004)
SHOWEX (November 1997)	508	10–49	1.9–12.1	Long-EZ, off coast of Virginia and North Carolina	Sun et al. (2001)
SHOWEX (March 1999)	199	8–48	3.4–17.3	Long-EZ, off coast of Virginia and North Carolina	Sun et al. (2001)
SHOWEX (November 1999)	970	3–48	0.5–16.5	Long-EZ, off coast of Virginia and North Carolina	Sun et al. (2001)
TOGA COARE	938	26–43	0.5–9.4	NCAR Electra, western equatorial Pacific Ocean	Sun et al. (1996)

We did only minimal initial screening of the aircraft data for quality control (cf. Mahrt et al. 2012). In low winds, wave effects or uncertainty in the aircraft turbulence measurements can produce a stress that appears upward, contrary to boundary layer theory. We screened for such spurious stress measurements and eliminated 662 cases from the initial 6080 flight legs summarized in Table 2. Over 95% of these questionable measurements occurred with flight-level winds of less than 8 m s^{-1}.

On the other hand, the original authors of the Janssen, Risø Air–Sea Experiment (RASEX), Southern Ocean Waves Experiment (SOWEX), and Surface Wave Dynamics Experiment (SWADE) data in Table 1 probably screened these datasets more strictly before publishing them and reported only "high quality" fluxes. Although the FASTEX, GFDex, and Humidity Exchange over the Sea (HEXOS) sets had been processed when we received them, we suspect that these sets had been screened only for instrument malfunctions—not for stationarity, homogeneity, wave characteristics, or other relevant quality metrics.

We further screened the SWADE set ourselves. The original set has 126 records; and Donelan et al. (1997) had identified whether each record represented conditions of wind sea or whether there was swell with wind in the same direction, in the opposing direction, or at right angles. In Fig. 1, we include only the 27 SWADE cases with wind sea; later we will discuss the remaining SWADE data that had swell present.

A distinct feature of all the data represented in Tables 1 and 2 is that they come from eddy-covariance measurements of the momentum and heat fluxes. We eschewed available datasets that were based on inertial-dissipation estimates of the fluxes because such fluxes rely heavily on Monin–Obukhov similarity theory. We want to minimize our reliance on similarity theory.

Initially in our analysis, we will treat the original and aircraft datasets separately. In effect, we are using the aircraft dataset to validate our analysis of the original dataset, or vice versa.

The method used for estimating U_{N10} for this work is crucial. One approach, obviously, is to use (1.8) and the measured u_*. The required z_0 could come from the corresponding measured value, from a lookup table or a comparable standard (e.g., Panofsky and Dutton 1984, 121–123; Stull 1988, p. 380; Wieringa 1993), or from a parameterization such as the Charnock relation. With that approach, however, the dependent variable in the analysis, the measured u_*, will be very well (and artificially) correlated with the independent variable U_{N10}.

To avoid such tautology, we start instead with (1.5). When our interest is in the wind speed at 10 m, we can rewrite (1.5) as

$$\frac{u_*}{k}\ln(10/z_0) \equiv U_{N10} = U(z) - \frac{u_*}{k}\ln(z/10) + \frac{u_*}{k}\psi_m(z/L). \tag{2.1}$$

That is, if we use the right-hand side of this equation to obtain U_{N10}, U_{N10} is most sensitive to the actual wind measurement, $U(z)$, and has generally only a modest built-in dependence on the measured u_*. Furthermore, if the measurement height is close to 10 m [when

$\ln(z/10) \sim 0$] and if the stratification is near neutral [when $\psi_m(z/L) \sim 0$], the U_{N10} obtained from (2.1) has very weak built-in correlation with u_*, and U_{N10} has nearly the same uncertainty as $U(z)$. A U_{N10} estimated from (1.8), in contrast, always has an uncertainty no smaller than the uncertainty in u_*.

When we could, we estimated U_{N10} from (2.1). For all the aircraft data in Table 2, this was the case. For ψ_m we used the function from Paulson (1970) in unstable stratification and the function from Grachev et al. (2007a) in stable stratification. For the FASTEX, GFDex, and RASEX data in Table 1, we had enough information to also calculate U_{N10} according to (2.1). In the CBLAST-hurricane set, U_{N10} was estimated with a stepped-frequency microwave radiometer (Drennan et al. 2007) and thus has no built-in dependence on u_*. In the HEXOS set, DeCosmo (1991) reported only U_{N10} and did not explain how she obtained this value. In the SOWEX set, Banner et al. (1999) obtained U_{N10} from (1.8). In the SWADE set, Donelan et al. (1997) reported U_{N10} and explained that they obtained it from (2.1).

Finally, Janssen (1997) reported only a variable denoted U_{10} but did not explain how this was obtained or whether it is the neutral-stability value. He did, however, report two simultaneous, independent sets of measurements: u_* and U_{10} were measured with both a pressure anemometer and a sonic anemometer. Under the assumption that U_{10} is U_{N10} but to avoid the built-in correlation in case Janssen estimated U_{N10} from (1.8), we switched the pressure anemometer and sonic measurements of u_* in our analysis. In other words, in Fig. 1 and subsequent figures, we plot u_* from the sonic against the corresponding U_{N10} value from the pressure anemometer and u_* from the pressure anemometer against the sonic U_{N10}. Now, in the Janssen set, the u_* and U_{N10} pairs have no direct built-in correlation from a shared u_*.

3. Results

Figure 2 is a plot like Fig. 1 but for the aircraft data summarized in Table 2. Unlike the original set, a high percentage of the aircraft data were collected in stable stratification—1123 of the 5418 data records left after our screening the stress. While we are not concerned about the flux divergence in unstable stratification for fluxes measured at the aircraft altitudes in this set (up to 49 m), we worry about possible flux divergence in stable stratification because of the generally shallower boundary layer. (Remember, we obtain the u_* surface value from the uncorrected momentum flux measured at flight level.)

To avoid biasing our analysis with u_* values biased low because of vertical flux divergence, we made several plots and analyses as in Fig. 2. Table 3 summarizes the calculations. First, we considered the aircraft data collected in unstable stratification and, separately, the data collected in stable stratification. Admittedly, the stable cases constituted only 26% as much data as in the unstable cases; still, as expected because of the flux divergence, the a value for the data collected in stable stratification is significantly less than the a value for the unstable cases.

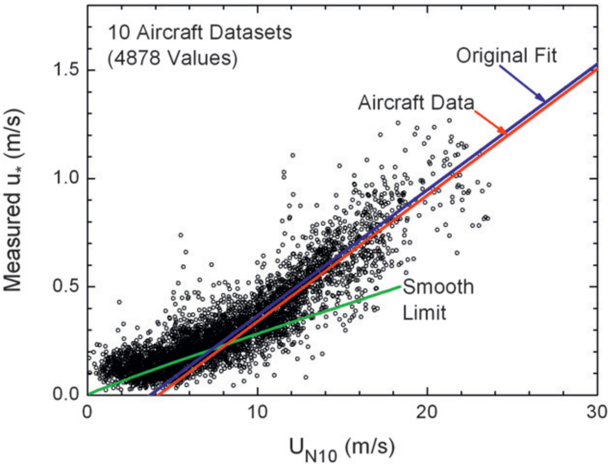

FIG. 2. As in Fig. 1, but these are all of the "aircraft" data (see Table 2) that were collected in unstable stratification and in stable stratification with $0 \le z/L \le 0.1$. The blue line is our fit to the original data in Fig. 1, (1.12); the red line is the fit to these data for $U_{N10} \ge 9\ \mathrm{m\,s^{-1}}$, (3.3).

Moreover, when we further segregated the stable data into cases with $0 \le z/L \le 0.1$ and with $0 \le z/L \le 0.2$, where z is the aircraft altitude and L is the measured Obukhov length, the set with the more stable conditions had a smaller a value than for the weakly stable set (Table 3). Finally, when we included just this weakly stable set (i.e., $0 \le z/L \le 0.1$) with all the unstable data, the resulting a and b values were indistinguishable from the a and b values for just the unstable data. Hence, as our analyzed "aircraft" dataset here, we use all the aircraft data collected in unstable stratification and the data from weakly stable stratification when $0 \le z/L \le 0.1$. This screening and the previously mentioned screening for stress reduced the original 6080 data records shown in Table 2 to 4878 records.

In both Figs. 1 and 2, the data clouds change character in the U_{N10} range 8–10 m s^{-1}. Below this range, the points have a shallower slope than above it. This tendency is compatible with aerodynamically smooth flow at low wind speeds and the transition to aerodynamically rough flow as the wind speed increases.

The roughness Reynolds number

$$R_* = \frac{u_* z_0}{\nu} \tag{3.1}$$

TABLE 3. Fits to the model $u_* = aU_{N10} + b$ for the original dataset and various configurations of the aircraft data. All cases use only data pairs for which $U_{N10} \geq 9$ m s^{-1}. The columns are the number of pairs in the fitting, the correlation coefficient r, the parameter a, the 95% confidence interval on a [from Bendat and Piersol (1971), p. 131], parameter b, and the 95% confidence interval on b.

Data source	Number	r	a	95% on a	b (m s^{-1})	95% on b (m s^{-1})
Original set	658	0.929	0.0581	[0.0564, 0.0599]	−0.214	[−0.239, −0.189]
All aircraft	1988	0.826	0.0584	[0.0567, 0.0602]	−0.252	[−0.275, −0.229]
Aircraft, all unstable	1680	0.835	0.0588	[0.0569, 0.0606]	−0.246	[−0.270, −0.221]
Aircraft, all stable	308	0.788	0.0512	[0.0467, 0.0557]	−0.223	[−0.279, −0.167]
Aircraft, $0 \leq z/L \leq 0.1$	215	0.846	0.0528	[0.0483, 0.0572]	−0.205	[−0.262, −0.148]
Aircraft, $0 \leq z/L \leq 0.2$	263	0.820	0.0508	[0.0465, 0.0551]	−0.198	[−0.252, −0.143]
Aircraft, all unstable, stable with $0 \leq z/L \leq 0.1$	1895	0.835	0.0583	[0.0566, 0.0600]	−0.243	[−0.266, −0.221]

characterizes the roughness regime of the flow, where ν is the kinematic viscosity of air. For $R_* \leq 0.135$ [see Andreas and Treviño (2000) for a discussion of this choice], the flow is aerodynamically smooth; for $R_* \geq 2.5$ (e.g., Kraus and Businger 1994, p. 145), the flow is aerodynamically rough. In between these limits, the flow is in transition.

Previously, Wu (1969, 1980), Melville (1977), Kraus and Businger (1994, p. 145), and Foreman and Emeis (2010), for instance, discussed what wind speed or friction velocity is required for the sea surface to become aerodynamically rough. Wu (1980), Kraus and Businger, and Foreman and Emeis based their analyses, however, on the assumption that the Charnock relation

$$z_0 = \frac{\alpha u_*^2}{g} \tag{3.2}$$

specifies the wave-related roughness length. Here, α is the Charnock parameter, $0.01 \leq \alpha \leq 0.02$. While Wu (1969) and Melville based their analyses on data, we revisit the discussion of aerodynamic regimes here because we have much more data than they had available.

Figures 3 and 4 show our evaluation of R_* for the two datasets. Each figure includes the individual values, bin averages in 1 m s^{-1} bins in U_{N10}, and bin medians. Because R_* values are approximately lognormally distributed, the proper bin average is computed as the geometric mean—as opposed to the arithmetic mean. If the R_* values were perfectly lognormal within a bin, the median would be the same as the geometric mean. Notice that in both figures the medians and geometric means are close.

Both figures show that, on average, the sea surface is not aerodynamically rough until U_{N10} is greater than 8 m s^{-1}. As a conservative estimate, we therefore used only the data for which $U_{N10} \geq 9$ m s^{-1} to determine the fitting lines in Figs. 1 and 2 and in Table 3. Equation (1.12) already gave our fit for Fig. 1; for Fig. 2, least squares linear regression yields (Table 3)

$$u_* = 0.0583U_{N10} - 0.243, \tag{3.3}$$

where u_* and U_{N10} are in meters per second. The correlation coefficient is 0.835.

Bendat and Piersol (1971, p. 131) explain that both the slope and intercept in (1.12) and (3.3) follow Student t distributions. We therefore calculated 95% confidence intervals on the slopes and intercepts fitted to the original and aircraft data in Figs. 1 and 2 (Table 3). For the slope in (1.12), the 95% confidence interval is [0.0564, 0.0599]; for the intercept, [−0.239, −0.189]. For the slope in (3.3), the 95% confidence interval is [0.0566, 0.0600]; for the intercept, [−0.266, −0.221].

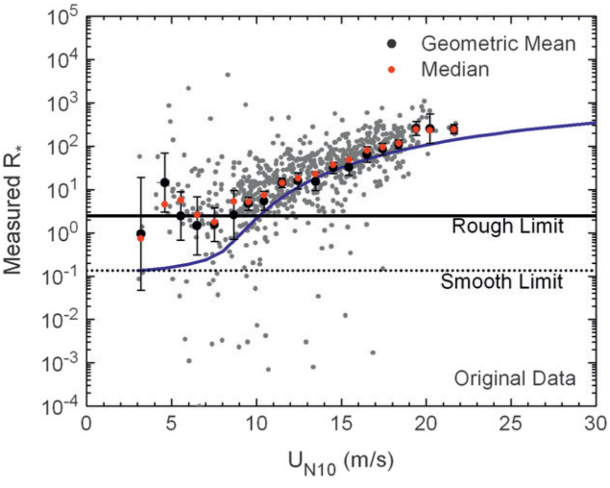

FIG. 3. Individual values of the measured roughness Reynolds number R_* (gray circles), from the original dataset (Table 1) are plotted against U_{N10}. The horizontal lines show the aerodynamically smooth limit (at 0.135) and the aerodynamically rough limit (at 2.5). The black circles are geometric means of the individual values within U_{N10} bins 1 m s^{-1} wide; the error bars are ±2 standard deviations in these bin means. The red circles are medians of the points within a bin. The blue line summarizes our analysis and derives from (3.1), (3.4), and (4.3).

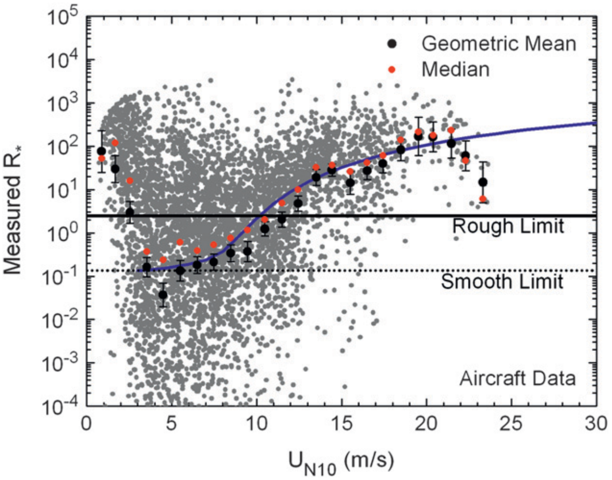

FIG. 4. As in Fig. 3, but for the aircraft data listed in Table 2.

Because both slope and intercept intervals coincide well, Figs. 1 and 2 give us essentially the same result. In effect, we validate the fitting line in Fig. 1 with Fig. 2, and vice versa. Henceforth, we will use the coefficients in (3.3) as our main result because they come from the larger dataset.

The very large R_* values at small U_{N10} in Figs. 3 and 4 are related to the ''pathological behavior'' in C_{DN10} for small U_{N10} that we mentioned earlier. The z_0 values used to create these figures came from the left-hand side of (2.1) [or, alternatively, from (1.5)]:

$$z_0 = 10\exp\left(\frac{-kU_{N10}}{u_*}\right). \qquad (3.4)$$

When both U_{N10} and u_* are small, their uncertainties often cause kU_{N10}/u_* to be unrealistically small. Consequently, z_0 is unrealistically large, and so is R_*.

The slope in (1.10) that Foreman and Emeis (2010) reported (0.051) is smaller than our values, and their intercept (-0.14 m s^{-1}) is larger. We suspect that, because they used $U_{N10} = 8$ m s^{-1} as the lower limit for aerodynamically rough flow in their analysis, they may have retained some data reflecting aerodynamic transition. Notice in Figs. 1 and 2 how the u_* values at lower winds turn up and away from (1.12) and (3.3). By including such data in their calculations, Foreman and Emeis would have inadvertently decreased *a* and increased *b* from what the data in truly rough flow suggest.

At $U_{N10} = 9$ m s^{-1}, (3.3) gives $u_* = 0.28$ m s^{-1}. In our analysis, this is the friction velocity at the transition to aerodynamically rough flow. For comparison, Wu (1969) concluded that this transition is at $U_{N10} = 7$ m s^{-1}, whereas Wu (1980) obtained $u_* = 0.263$ m s^{-1}, although he assumed $R_* = 2.33$ at the transition to aerodynamically rough flow. From his data analysis, Melville (1977) concluded that u_* was in the range 0.15–0.30 m s^{-1} at the onset of aerodynamically rough flow, although he also used for the transition an R_* limit (=2) lower than ours. On invoking the Charnock relation, Kraus and Businger (1994, p. 145) and Foreman and Emeis (2010) estimated u_* was 0.29 and 0.28 m s^{-1}, respectively, at the transition to aerodynamically rough flow.

Hence, our estimate that $u_* = 0.28$ m s^{-1} at the transition to aerodynamically rough flow agrees with most previous estimates; but our result that $U_{N10} = 9$ m s^{-1} at this transition is a bit higher than previous estimates.

4. Discussion

a. *Consistency of the results*

Thoughtful readers might suspect that the data clouds in Figs. 1 and 2 obscure differences in behavior among the different datasets that are typical in plots of C_{DN10} versus U_{N10}. Then our fitting lines in Figs. 1 and 2 would just be average results that ignore true differences in drag relations among the sets. To allay these worries, we created Figs. 5 and 6.

These show the individual datasets that went into Figs. 1 and 2. Figure 5 shows our original data; Fig. 6, the aircraft data. Reassuringly, 17 of the 18 datasets individually either lie along our aircraft fit, (3.3), suggest aerodynamically smooth scaling at low wind speed, or do both. That is, the individual datasets are not biased high or low such that, when we fitted (1.10) to the two consolidated datasets, the fitting line simply split the difference between systematically high and systematically low values.

The one exception to this behavior is the CBLAST hurricane dataset (Fig. 5). These u_* values seem to be too low—probably for the reasons we discussed earlier. We have therefore not included them in our least squares fittings.

b. *A unified roughness parameterization*

The green lines in Figs. 1, 2, 5, and 6 show aerodynamically smooth scaling, where the roughness length is

$$z_{0s} = 0.135\frac{\nu}{u_*}. \qquad (4.1)$$

Andreas and Treviño (2000) (cf. Andreas et al. 2008, 2010) explain our choice of the coefficient 0.135.

Because these green lines are virtually linear from $U_{N10} = 0$ to where they intersect our aerodynamically rough results, (1.12) and (3.3), we fitted them with

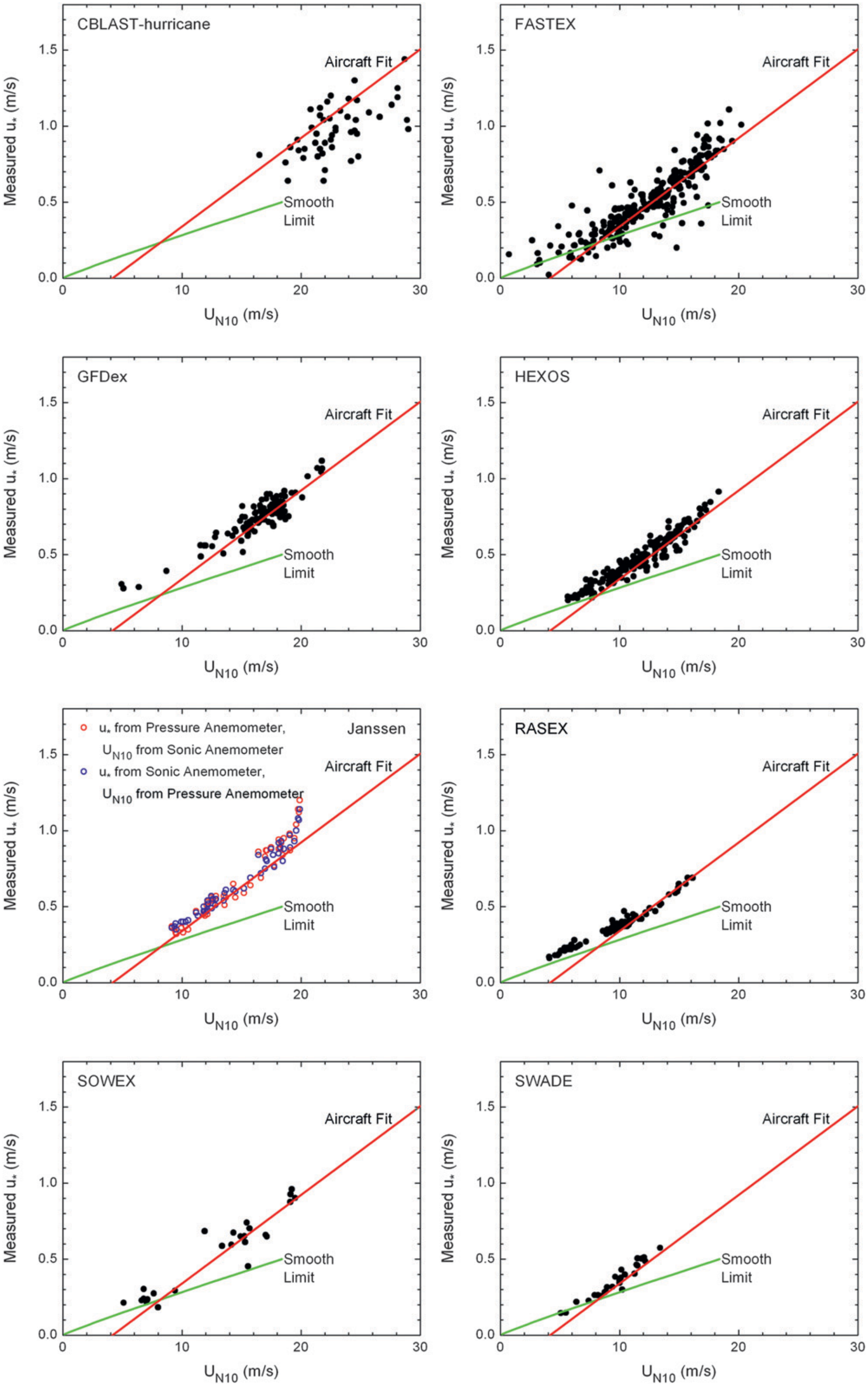

FIG. 5. Each dataset listed in Table 1 is plotted individually as u_* vs U_{N10}. In each panel, the red line is the fit to the aircraft data, (3.3). The green line shows the aerodynamically smooth limit, (4.1). The Janssen plot is different from the others because Janssen (1997) reported simultaneous measurements of u_* and U_{N10} with both a sonic anemometer and a pressure anemometer. As discussed in the text, to avoid artificial correlation in this dataset, we paired the sonic U_{N10} with the pressure anemometer u_*, and vice versa.

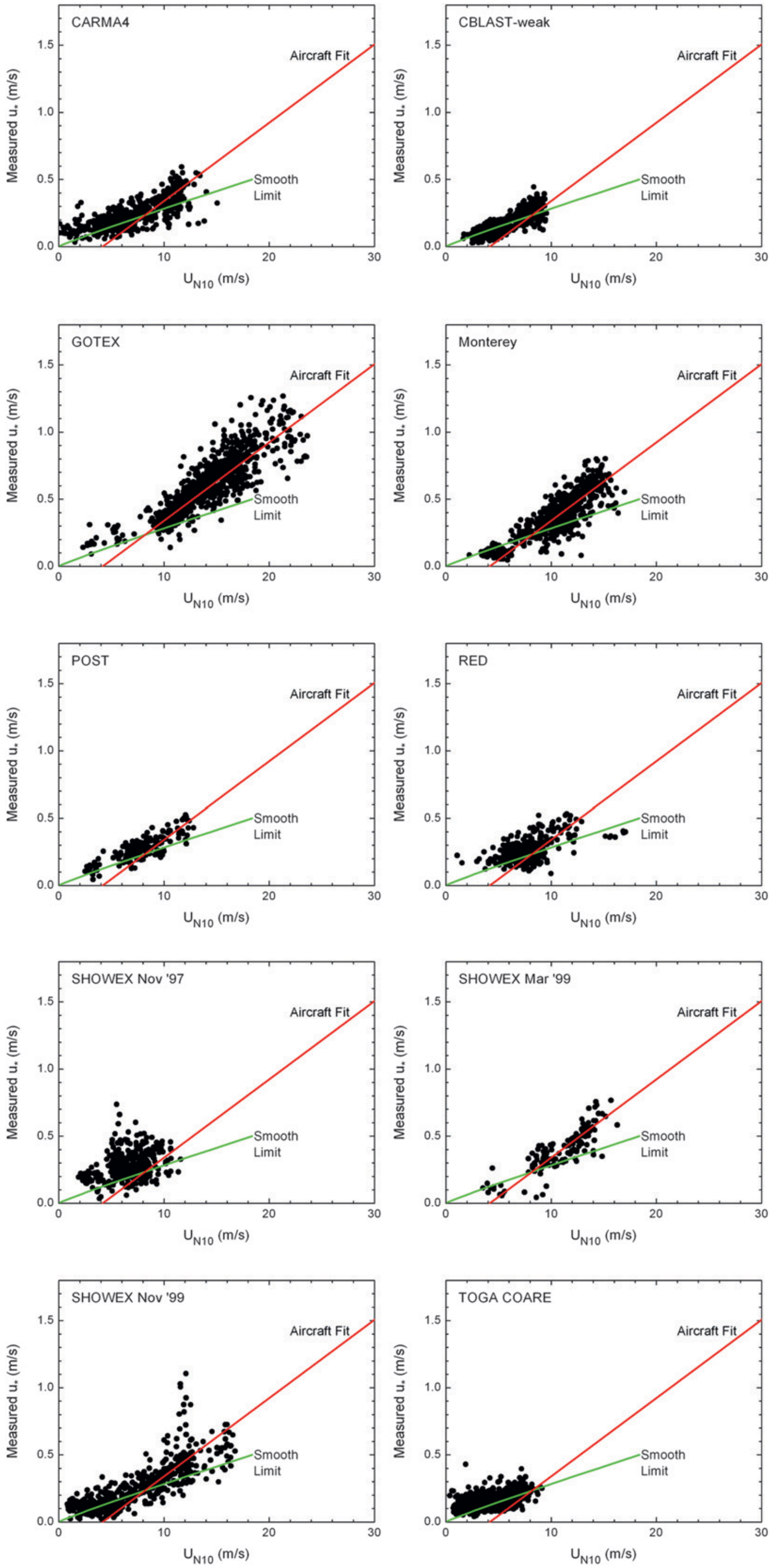

FIG. 6. As in Fig. 5, but for the individual datasets in the aircraft set (Table 2).

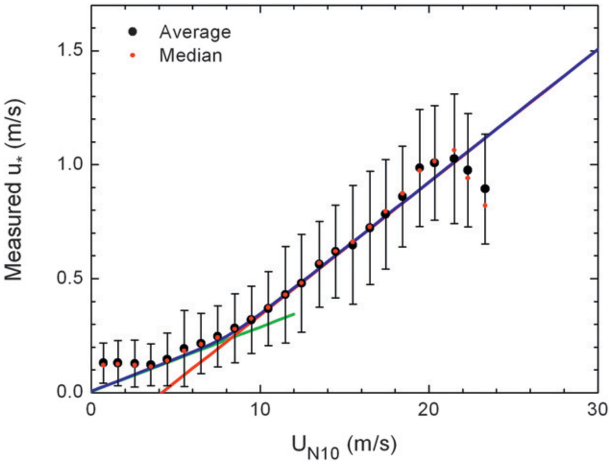

FIG. 7. The u_* values from the original and aircraft datasets are combined and averaged in U_{N10} bins 1 m s^{-1} wide. The red points are medians in these bins; the error bars are ±2 standard deviations in the bin populations. As in earlier figures, the green line shows the aerodynamically smooth limit, (4.1), and the red line is our fit to the aircraft data, (3.3). The blue curve is a hyperbola that smoothly joins these two lines, (4.3).

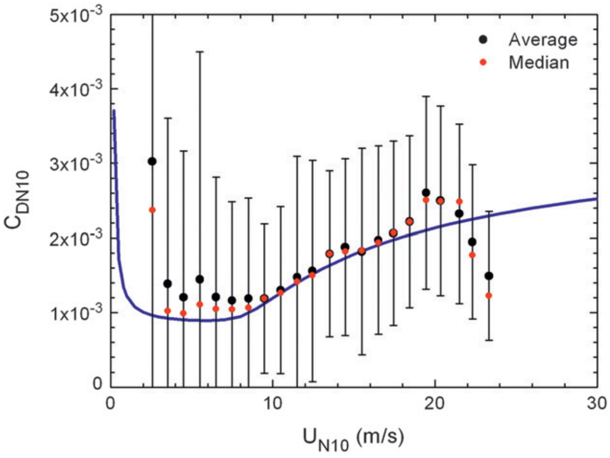

FIG. 8. The C_{DN10} values from the combined original and aircraft datasets—computed as $(u_*/U_{N10})^2$—are averaged in U_{N10} bins 1 m s^{-1} wide. The red points are medians in these bins; the error bars are ±2 standard deviations in the bin populations. The blue curve is our unified expression for C_{DN10}, obtained by inserting (4.3) into (1.9).

$$u_* = 0.0283U_{N10} + 0.005\,13. \tag{4.2}$$

This line is appropriate for U_{N10} in [0, 8.76 m s^{-1}].

Two intersecting lines now describe our results, (3.3) and (4.2). We can therefore represent u_* with a smooth, differentiable function of U_{N10} by combining (3.3) and (4.2) in a hyperbola. The result that best fits our data for all U_{N10} is

$$\begin{aligned} u_* = {} & 0.239 + 0.0433\{(U_{N10} - 8.271) \\ & + [0.120(U_{N10} - 8.271)^2 + 0.181]^{1/2}\}, \end{aligned} \tag{4.3}$$

where u_* and U_{N10} are both in meters per second.

Figure 7 shows how well this expression fits the bin-averaged u_* values from the combined original and aircraft datasets. Only for $U_{N10} < 3$ m s^{-1} do the data in Fig. 7 deviate significantly from (4.3). Instead of highlighting missing physics, these three large u_* values reveal how difficult measuring u_* is in low winds.

Equation (4.3) now becomes a core component of a new bulk flux algorithm that we are developing. The appendix sketches how we use (4.3) in this algorithm.

For readers used to looking at flux algorithms in terms of C_{DN10}, we can insert (4.3) into (1.9) to obtain an expression for C_{DN10} for all wind speeds. Figure 8 shows this result and how it fits the bin-averaged C_{DN10} values in our combined original and aircraft datasets.

Figures 7 and 8 also reiterate some of the advantages of a drag relation based on u_* over one based on C_{DN10} that we described in the introduction. Although the averaged u_* values in the three lowest U_{N10} bins in Fig. 7 do not follow aerodynamically smooth scaling, at least they are well behaved and have some of the smallest error bars in the plot. The C_{DN10} values in the two lowest U_{N10} bins in Fig. 8, in contrast, are above the upper limit of the plot and thus do not show up at all. Moreover, the errors bars on the C_{DN10} values for small U_{N10} are generally the largest on the plot and even encompass negative C_{DN10} values.

Figure 8 also suggests that the distribution of individual C_{DN10} values within bins is skewed toward larger values: For $U_{N10} < 9$ m s^{-1}, the averages are larger than the medians. In Fig. 7, (4.3) fits the bin-averaged u_* values very well. In contrast, the bin-averaged C_{DN10} values for $U_{N10} < 9$ m s^{-1} in Fig. 8 are above the C_{DN10} curve derived from (4.3) although the same data as in Fig. 7 went into this plot. All of these features are evidence of what we termed pathological behavior in C_{DN10}.

c. Drag relations in high winds

Figure 9 shows (4.3) extrapolated to hurricane-strength winds. The figure also shows both the original and aircraft datasets to emphasize how consistent they are. Furthermore, Fig. 9 includes the CBLAST hurricane data to demonstrate that they are generally below reliable data measured at similar wind speeds.

The main features of Fig. 9, however, are the curves attributed to Moon et al. (2007) and Mueller and Veron (2009). These are theoretical results in which both sets of authors modeled the total wind stress on the sea as a combination of the viscous stress (or skin friction or

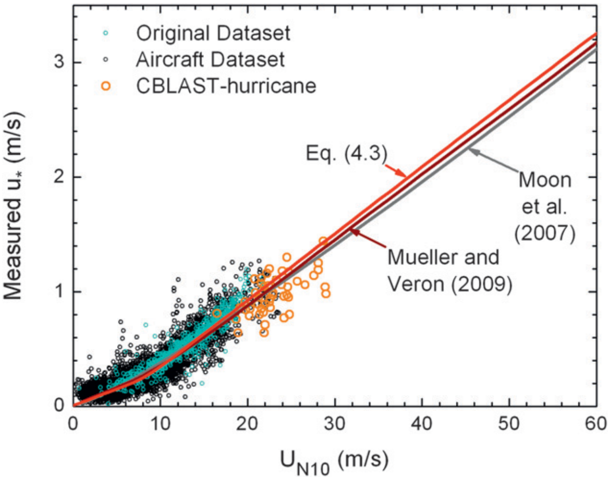

FIG. 9. All of the original and aircraft data in Tables 1 and 2 are replotted, as are the CBLAST hurricane data from Table 1. The red line shows the fit that we use as our main result, (4.3). The two other curves are theoretical results from Moon et al. (2007) and Mueller and Veron (2009) for winds up to at least 70 m s^{-1}. The Mueller and Veron curve is for a fetch 100 km long, water temperature 27°C, air temperature 26°C, and relative humidity 90%.

tangential stress), a wave-induced stress from form drag, and the reduction of the viscous and wave-induced stresses by sheltering (or flow separation).

Moon et al. (2007) obtained their results [summarized in their (4) and (5)] by simulating the surface stress in 10 Atlantic hurricanes with wind speeds up to 70 m s^{-1} using the hurricane model of Moon et al. (2004). They then inferred z_0 from this modeled stress through similarity theory. Their z_0 values are thus statistical averages in wind speed bins. The Mueller and Veron (2009) model, on the other hand, simply provides a deterministic prediction of the surface stress for the given input conditions. [F. Veron (2011, personal communication) reran the Mueller and Veron model for our specified conditions for wind speeds up to 80 m s^{-1}.] Neither group evidently realized that its model yielded a nearly straight-line relation between u_* and U_{N10} for U_{N10} above 20–25 m s^{-1} (Fig. 9). We use this theoretical behavior in these two models to justify extrapolating our own result, (4.3), to hurricane-strength winds.

We cast our results in the familiar form of a drag coefficient in Fig. 10. Remember, because of (1.11), our drag coefficient rolls off and approaches an asymptotic limit of a^2 in high winds: 3.40×10^{-3}. Figure 10 also shows the Moon et al. (2007) and Mueller and Veron (2009) results and the "Charnock + Smooth" curve, which we obtain by adding (4.1) and the Charnock relation, (3.2) [with $\alpha = 0.0185$, Andreas et al. (2008)], to get a unified expression for z_0 (e.g., Zilitinkevich 1969; Smith 1988; Fairall et al. 1996).

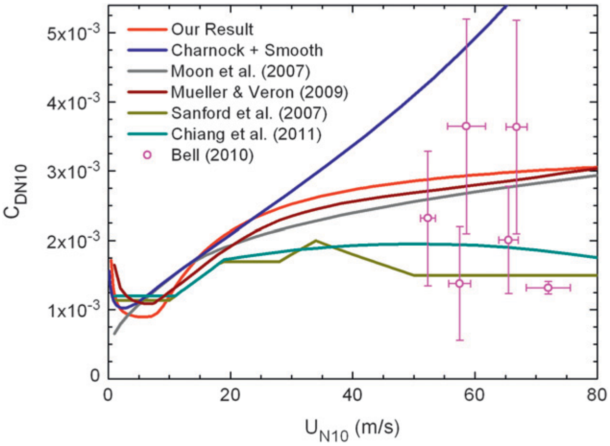

FIG. 10. Several opinions as to the 10-m, neutral-stability drag coefficient C_{DN10} as a function of U_{N10}. "Our result" comes from (4.3). The Moon et al. (2007) and Mueller and Veron (2009) curves are just recast as drag coefficients from Fig. 9. The "Charnock + Smooth" curve comes from adding the aerodynamically smooth roughness, (4.1), and the Charnock relation, (3.2). The Sanford et al. (2007) and Chiang et al. (2011) curves are their adaptations of the results from Powell et al. (2003) for use in their mixed-layer models. Bell's (2010) data come from estimates of the angular momentum budget in Hurricanes Fabian and Isabel.

In models of the oceanic mixed layer under hurricanes, both Sanford et al. (2007) and Chiang et al. (2011) based parameterizations for C_{DN10} on the observations reported by Powell et al. (2003). While we do not endorse the Powell et al. results for several reasons, we show in Fig. 10 the Sanford et al. and Chiang et al. C_{DN10} parameterizations because they are continuous functions, like the other curves in Fig. 10, and because, we feel, they represent the lowest reasonable drag coefficient possible in high winds.

Finally, Fig. 10 also includes the drag coefficients that Bell (2010) obtained by using dropsondes launched in Hurricanes Fabian and Isabel in 2003 to estimate the angular momentum budget under the assumption that the storms were axisymmetric. These are the most recent determinations of air–sea drag in high winds that are available. Bell computed drag coefficients for six separate aircraft missions and used 72 control volumes per mission for flux calculations. The error bars on his points in Fig. 10 are thus (probably) standard deviations around the means of the 72 samples per mission. That is, they are not uncertainty estimates but rather indicators of the scatter in the individual values.

Bell's (2010) results, unfortunately, do not help us decide which of the candidate drag parameterizations in Fig. 10 is the most realistic. His data range from below the lowest realistic parameterization to above our parameterization, which we suggest gives the greatest upper bound.

Ingel (2011) refers to the rolloff in C_{DN10} depicted in Fig. 10 as a ''drag crisis,'' invoking the terminology of classical fluid mechanics when laminar flow transitions to turbulence and the drag coefficients of cylinders and spheres drop suddenly by a factor of 5 with increasing Reynolds number (Monin and Yaglom 1971, 82–83; Faber 1995, 266–267). That is, according to Ingel, something fundamental about the air–sea coupling has changed. Kudryavtsev (2006) believes that this rolloff signals a saturation of the surface stress: the stress no longer increases with increasing wind speed. Neither of these inferences is true.

If u_* is a *linear* function of U_{N10} for moderate and high wind speeds—as our data and the theories of Moon et al. (2007) and Mueller and Veron (2009) suggest—nothing fundamental changes about the way air and sea couple as the wind speed increases. There is certainly no drag crisis in the classical sense. Nor does the surface stress saturate: (3.3) confirms that u_* and thus the surface stress increase with wind speed for all wind speeds.

The roughness length does saturate, however, as Donelan et al. (2004) suggest. From (3.3) and (3.4), we see that z_0 approaches a limiting value of 1.05×10^{-2} m [$=10 \exp(-k/a)$] at large U_{N10}.

Because Moon et al. (2007) and Mueller and Veron (2009) account for the behavior that we see in the data by modeling just wind–wave coupling, invoking more exotic processes to explain the rolloff in C_{DN10} seems unnecessary. Many of these attempts to explain the rolloff in C_{DN10} involve injecting sea spray into the near-surface air in copious amounts (e.g., Makin 2005; Kudryavtsev 2006; Soloviev and Lukas 2010; Ingel 2011; Bianco et al. 2011). Such spray loading may stabilize the near-surface air and thus reduce the momentum transfer somewhat in very high winds.

Shpund et al. (2011) recently suggested, however, that such spray loading may not be as important as has been estimated from one-dimensional, eddy-diffusivity models (e.g., Lighthill 1999; Makin 2005; Kudryavtsev 2006; Ingel 2011; Bianco et al. 2011). When Shpund et al. introduced large eddies into their two-dimensional Lagrangian model, these eddies carried spray that was generated at the sea surface to higher levels in the marine boundary layer, thereby reducing the spray loading near the surface.

Still, we cannot rule out the possibility that, with increasing wind speed, spray loading may cause the actual drag relation to fall slightly below our result in Fig. 10. Nevertheless, wind–wave coupling appears to be the dominant mechanism causing the drag coefficient to roll off.

d. *Effects of sea state*

The idea that the roughness of the sea surface z_0 may depend on wave age C_p/u_*, where C_p is the phase speed of the dominant waves, goes back at least to Kitaigorodskii and Volkov (1965). Many authors have investigated whether this and other sea-state parameters influence air–sea drag (e.g., Smith et al. 1992; Janssen 1997; Bourassa et al. 2001; Oost et al. 2002; Drennan et al. 2005). Jones and Toba (2001) dedicated an entire book to this subject of how to parameterize the drag; in that book, Toba et al. (2001) highlighted the fact that ''there is still lively debate'' on this issue of how sea state influences the air–sea drag.

Briefly, the question is whether an air–sea drag parameterization can be successful as a function of just wind speed or whether it must also include sea-state variables such as wave age, wave height, wave period, or swell height and direction. Although our drag parameterization for aerodynamically rough flow requires only U_{N10}, we cannot conclude that sea state is unimportant. After all, our extrapolated drag relation for aerodynamically rough flow, (4.3), corroborates the model predictions of Moon et al. (2007) and Mueller and Veron (2009) (Figs. 9 and 10), which involved integrating the ocean wave spectrum. Because these models depend implicitly on wave age, wave height, and wave steepness through the wave spectrum, our results, in turn, imply that these parameters are important for air–sea coupling.

The SWADE dataset (Table 1), which includes observations of swell, also has implications for our parameterization. Remember that, in the SWADE set, Donelan et al. (1997) noted whether their measurements of surface stress were made over a wind sea or in the presence of swell that was across wind, counter to the wind, or following the wind. Figure 11 shows the full SWADE dataset, plotted as u_* versus U_{N10}, with these four regimes identified.

Although we add only 99 points to our analysis, Fig. 11 suggests how robust our u_*-versus-U_{N10} analysis is and how weakly swell affects the drag. For most of the U_{N10} range, the swell cases on average have u_* values only 10%–15% higher than the wind sea cases. At the upper end of the U_{N10} range, however, the swell and wind sea cases are essentially coincident (cf. Drennan et al. 2003). Only for the lowest U_{N10} values—well below the aerodynamically rough regime ($U_{N10} < 9$ m s^{-1})—do swell cases deviate significantly from the wind sea cases and from the central tendency of our analysis.

We hypothesize that, in moderate and high winds, the sea surface is so strongly forced by the wind that swell has a low-order effect on the surface stress. In light winds, on the other hand, the relationship between wind stress and swell becomes significant.

Still, the observed erratic behavior of the drag in light winds—expressed as the drag coefficient C_{DN10}, the roughness length z_0, or u_* (Figs. 7, 8, and 11; e.g.,

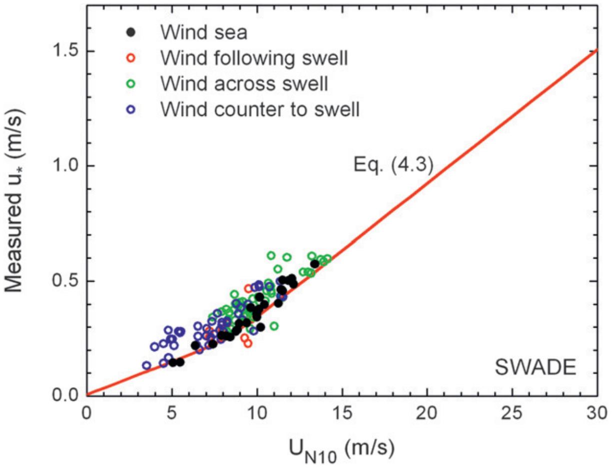

FIG. 11. All of the SWADE data (Table 1) are plotted as u_* vs U_{N10}. Here, to the wind-sea-only data shown in Figs. 1, 5, and 9, we add measurements with swell in three categories: wind across the swell, wind following the swell, and wind counter to the swell. The red line is our main result, (4.3).

Rutgersson et al. 2001; Drennan et al. 2003)—may simply reflect how difficult defining a meaningful reference frame and then measuring stress is in light winds with swell present. In fact, with swell opposing a light wind, the ocean may actually drag the atmosphere (e.g., Smedman et al. 1994; Grachev and Fairall 2001; Grachev et al. 2003).

5. Conclusions

Despite many measurements, the drag coefficient formulated as $C_{DN10} = (u_*/U_{N10})^2$ —a legacy from laboratory fluid mechanics—still has wide variability at low and moderate wind speeds. For hurricane-strength winds, it is uncertain by a factor of 3 (Fig. 10). We discussed several reasons why C_{DN10} is naturally prone to such variability. Here, we therefore evaluated an alternative formulation of the air–sea drag relation, following the suggestion by Foreman and Emeis (2010).

Using seven times as much data as Foreman and Emeis (2010) used, we confirm their main conclusion that the friction velocity u_*, measured over the ocean in aerodynamically rough flow increases linearly with U_{N10}, the 10-m, neutral-stability wind speed. We find

$$u_* = 0.0583U_{N10} - 0.243, \qquad (5.1)$$

Not only do our two independent datasets, comprising 7 and 10 individual datasets, respectively, follow this relation, but each individual set that includes data for which $U_{N10} \geq 9\ \mathrm{m\ s^{-1}}$ follows it. Such consistent behavior is never found in plots of C_{DN10}.

The significant part of our analysis is that this new relation has a negative intercept. Consequently, the 10-m, neutral-stability drag coefficient rolls off and asymptotes to a constant in high winds:

$$C_{DN10} \equiv \left(\frac{u_*}{U_{N10}}\right)^2 = 3.40 \times 10^{-3}\left(1 - \frac{4.17}{U_{N10}}\right)^2. \qquad (5.2)$$

This behavior is exactly what hurricane modelers have been trying to justify and theorists have been trying to explain.

We suggest that wind–wave coupling explains (5.1). Theoretical models for the surface stress by Moon et al. (2007) and Mueller and Veron (2009) include terms for only the skin friction, form drag on the waves, and flow sheltering. Yet, these produce nearly straight-line relations between u_* and U_{N10} up to winds of major hurricane strength. (Neither group evidently realized this behavior.) Furthermore, both model predictions are very close to our (5.1). As a result, we conclude that known processes involving wind–wave coupling may be enough to explain the behavior of the air–sea drag for all wind speeds. These theoretical results also motivate our extrapolating (5.1) to hurricane-strength winds.

The literature contains data-based estimates that suggest C_{DN10} can be as low as 1.5×10^{-3} in 50 m s^{-1} winds (e.g., Powell et al. 2003). We believe that this estimate is the smallest lower bound on the drag coefficient in hurricane-strength winds. On the other hand, one way to view our result (5.2) is as the greatest upper bound on the drag coefficient.

Processes that the models of Moon et al. (2007) and Mueller and Veron (2009) did not include—such as spray loading—may reduce the drag coefficient from what (5.2) predicts. We hypothesize, however, that any such effects will be second order, reducing C_{DN10} from the level in (5.2) by, perhaps, 10%. Because the sea surface is so strongly forced in high winds, we also hypothesize that swell will negligibly affect air–sea drag for wind speeds above ~15 m s^{-1}.

From the behavior of the roughness Reynolds number in our two datasets, we also estimated the wind speed and the friction velocity at which the sea surface becomes aerodynamically rough. Although the roughness Reynolds numbers are scattered, we have enough data to reliably determine mean behavior. We conclude that the sea surface becomes aerodynamically rough for U_{N10} between 8 and 10 m s^{-1}; as an operational estimate, we use $U_{N10} = 9\ \mathrm{m\ s^{-1}}$ as the wind speed at transition. From (5.1), this wind speed gives $u_* = 0.28\ \mathrm{m\ s^{-1}}$ as the friction velocity when the sea surface becomes aerodynamically rough.

Although flux measurements at sea in light winds have larger uncertainty, our data suggest that u_* follows aerodynamically smooth scaling at low U_{N10}, where the roughness length is presumed to obey $z_{0s} = 0.135(\nu/u_*)$. For $U_{N10} < 9\ \mathrm{m\ s^{-1}}$, this expression produces nearly straight-line behavior in plots of u_* versus U_{N10}. We thus fitted this smooth region with a straight line, (4.2), to complement our straight-line result in rough flow, (5.1).

It was then natural to smoothly join these two straight lines with a hyperbola that constitutes a unified drag parameterization that encompasses weak-to-strong winds:

$$u_* = 0.239 + 0.0433\{(U_{N10} - 8.271) + [0.120(U_{N10} - 8.271)^2 + 0.181]^{1/2}\}. \quad (5.3)$$

Here, u_* and U_{N10} are in meters per second.

Acknowledgments. We thank the following colleagues for providing datasets: Will Drennan and Jun Zhang for the CBLAST-hurricane set; Ola Persson, Jeff Hare, Chris Fairall, and Bill Otto for the FASTEX set; Nína Petersen and Ian Renfrew for the GFDex set; and Janice DeCosmo for help with the HEXOS set. We thank Fabrice Veron for rerunning the Mueller and Veron (2009) model to produce the curves we show in Figs. 9 and 10 and Emily Moynihan for preparing Figs. 5 and 6. Two anonymous reviewers made insightful comments that helped us focus the manuscript better. The U.S. Office of Naval Research supported this work with Award N00014-11-1-0073 to NorthWest Research Associates. ONR also supported ELA through the National Ocean Partnership Program with Award N00014-10-1-0154 to the University of Rhode Island, for whom he is a subcontractor.

APPENDIX

Bulk Flux Algorithm

A motivation for our developing the u_* parameterization (4.3) was to use it in a bulk flux algorithm for high-wind, spray conditions. Sea spray enhances the air–sea exchange of sensible and latent heat; consequently, in such an algorithm, the total sensible ($H_{s,T}$) and latent ($H_{L,T}$) heat fluxes each include two terms, an *interfacial* part (H_s and H_L) and a *spray-mediated* part ($Q_{s,\mathrm{sp}}$ and $Q_{L,\mathrm{sp}}$) (Andreas et al. 2008; Andreas 2011a). With the surface stress or momentum flux, τ, the bulk flux algorithm thus comprises three main equations:

$$\tau = \rho_a u_*^2, \quad \text{(A1a)}$$

$$H_{s,T} = H_s + Q_{s,\mathrm{sp}}, \quad \text{(A1b)}$$

$$H_{L,T} = H_L + Q_{L,\mathrm{sp}}. \quad \text{(A1c)}$$

Equation (4.3) goes directly into (A1a) and provides τ once U_{N10} is calculated from (2.1). Andreas et al. (2008) give the equations for computing $Q_{s,\mathrm{sp}}$ and $Q_{L,\mathrm{sp}}$, which also depend on u_*. Our specifying u_* directly from U_{N10}, however, allows us to deviate from standard methods for calculating the interfacial fluxes H_s and H_L.

By definition, these are

$$H_s = -\rho_a c_p u_* \theta_*, \quad \text{(A2a)}$$

$$H_L = -\rho_a L_v u_* q_*. \quad \text{(A2b)}$$

Here c_p is the specific heat of air at constant pressure, L_v is the latent heat of vaporization, and θ_* and q_* are temperature and specific humidity flux scales analogous to u_*. These θ_* and q_*, in turn, appear in the Monin–Obukhov similarity expressions for the profiles of average potential temperature Θ and specific humidity Q in the atmospheric surface layer (Garratt 1992, 52–54; Andreas et al. 2008):

$$\Theta_r = \Theta_s + \frac{\theta_*}{k}[\ln(r/z_T) - \psi_h(r/L)], \quad \text{(A3a)}$$

$$Q_r = Q_s + \frac{q_*}{k}[\ln(r/z_Q) - \psi_h(r/L)]. \quad \text{(A3b)}$$

In these, r is a reference height; Θ_r and Q_r are thus the average potential temperature and specific humidity at height r; Θ_s and Q_s are the corresponding values at the sea surface. Also, L is the Obukhov length—a function of u_*, θ_*, and q_*. For the stability correction ψ_h, we use the same sources that we did for the ψ_m function in (2.1): Paulson (1970) for unstable stratification, and Grachev et al. (2007a) for stable stratification. Andreas et al. (2008) explain how we estimate the roughness lengths z_T and z_Q.

Rearranging (A3) and inserting them, respectively, into (A2) yields our algorithm for the interfacial heat fluxes:

$$H_s = \frac{\rho_a c_p k u_* (\Theta_s - \Theta_r)}{\ln(r/z_T) - \psi_h(r/L)}, \quad \text{(A4a)}$$

$$H_L = \frac{\rho_a L_v k u_* (Q_s - Q_r)}{\ln(r/z_Q) - \psi_h(r/L)}. \quad \text{(A4b)}$$

As usual, (A1a) and (A4) must be solved iteratively because these and U_{N10}, (2.1), are coupled through the Obukhov length.

Notice that this new algorithm requires no parameterization for z_0, which is one of the most variable and uncertain quantities in surface layer similarity theory.

REFERENCES

Anderson, K., and Coauthors, 2004: The RED Experiment: An assessment of boundary layer effects in a trade winds regime on microwave and infrared propagation over the sea. *Bull. Amer. Meteor. Soc.,* **85,** 1355–1365.

Andreas, E. L, 2011a: Fallacies of the enthalpy transfer coefficient over the ocean in high winds. *J. Atmos. Sci.,* **68,** 1435–1445.

——, 2011b: The fallacy of drifting snow. *Bound.-Layer Meteor.,* **141,** 333–347.

——, and G. Treviño, 2000: Comments on "A physical interpretation of von Kármán's constant based on asymptotic considerations—A new value." *J. Atmos. Sci.,* **57,** 1189–1192.

——, P. O. G. Persson, and J. E. Hare, 2008: A bulk turbulent air–sea flux algorithm for high-wind, spray conditions. *J. Phys. Oceanogr.,* **38,** 1581–1596.

——, ——, R. E. Jordan, T. W. Horst, P. S. Guest, A. A. Grachev, and C. W. Fairall, 2010: Parameterizing turbulent exchange over sea ice in winter. *J. Hydrometeor.,* **11,** 87–104.

Banner, M. L., W. Chen, E. J. Walsh, J. B. Jensen, S. Lee, and C. Fandry, 1999: The Southern Ocean Waves Experiment. Part I: Overview and mean results. *J. Phys. Oceanogr.,* **29,** 2130–2145.

Batchelor, G. K., 1970: *An Introduction to Fluid Dynamics.* Cambridge University Press, 615 pp.

Bell, M. M., 2010: Air–sea enthalpy and momentum exchange at major hurricane wind speeds. Ph.D. dissertation, Naval Postgraduate School, 133 pp.

Bendat, J. S., and A. G. Piersol, 1971: *Random Data: Analysis and Measurement Procedures.* Wiley-Interscience, 407 pp.

Bianco, L., J.-W. Bao, C. W. Fairall, and S. A. Michelson, 2011: Impact of sea-spray on the atmospheric surface layer. *Bound.-Layer Meteor.,* **140,** 361–381.

Blanc, T. V., 1985: Variation of bulk-derived surface flux, stability, and roughness results due to the use of different transfer coefficient schemes. *J. Phys. Oceanogr.,* **15,** 650–669.

Bourassa, M. A., D. G. Vincent, and W. L. Wood, 2001: A sea state parameterization with nonarbitrary wave age applicable to low and moderate wind speeds. *J. Phys. Oceanogr.,* **31,** 2840–2851.

Caughey, S. J., J. C. Wyngaard, and J. C. Kaimal, 1979: Turbulence in the evolving stable boundary layer. *J. Atmos. Sci.,* **36,** 1041–1052.

Chiang, T.-L., C.-R. Wu, and L.-Y. Oey, 2011: Typhoon Kai-Tak: An ocean's perfect storm. *J. Phys. Oceanogr.,* **41,** 221–233.

Crawford, T. L., and R. J. Dobosy, 1992: A sensitive fast-response probe to measure turbulence and heat flux from any airplane. *Bound.-Layer Meteor.,* **59,** 257–278.

DeCosmo, J., 1991: Air–sea exchange of momentum, heat and water vapor over whitecap sea states. Ph.D. dissertation, University of Washington, 212 pp.

Donelan, M. A., W. M. Drennan, and K. B. Katsaros, 1997: The air–sea momentum flux in conditions of wind sea and swell. *J. Phys. Oceanogr.,* **27,** 2087–2099.

——, B. K. Haus, N. Reul, W. J. Plant, M. Stiassnie, H. C. Graber, O. B. Brown, and E. S. Saltzman, 2004: On the limiting aerodynamic roughness of the ocean in very strong winds. *Geophys. Res. Lett.,* **31,** L18306, doi:10.1029/2004GL019460.

Drennan, W. M., H. C. Graber, D. Hauser, and C. Quentin, 2003: On the wave age dependence of wind stress over pure wind seas. *J. Geophys. Res.,* **108,** 8062, doi:10.1029/2000JC000715.

——, P. K. Taylor, and M. J. Yelland, 2005: Parameterizing the sea surface roughness. *J. Phys. Oceanogr.,* **35,** 835–848.

——, J. A. Zhang, J. R. French, C. McCormick, and P. G. Black, 2007: Turbulent fluxes in the hurricane boundary layer. Part II: Latent heat flux. *J. Atmos. Sci.,* **64,** 1103–1115.

Edson, J., and Coauthors, 2007: The Coupled Boundary Layers and Air–Sea Transfer Experiment in low winds. *Bull. Amer. Meteor. Soc.,* **88,** 341–356.

Emanuel, K. A., 1995: Sensitivity of tropical cyclones to surface exchange coefficients and a revised steady-state model incorporating eye dynamics. *J. Atmos. Sci.,* **52,** 3969–3976.

Faber, T. E., 1995: *Fluid Dynamics for Physicists.* Cambridge University Press, 440 pp.

Fairall, C. W., E. F. Bradley, D. P. Rogers, J. B. Edson, and G. S. Young, 1996: Bulk parameterization of air-sea fluxes for Tropical Ocean–Global Atmosphere Coupled Ocean–Atmosphere Response Experiment. *J. Geophys. Res.,* **101,** 3747–3764.

Foreman, R. J., and S. Emeis, 2010: Revisiting the definition of the drag coefficient in the marine atmospheric boundary layer. *J. Phys. Oceanogr.,* **40,** 2325–2332.

Francis, J. R. D., 1954: Wind stress on a water surface. *Quart. J. Roy. Meteor. Soc.,* **80,** 438–443.

French, J. R., W. M. Drennan, J. A. Zhang, and P. G. Black, 2007: Turbulent fluxes in the hurricane boundary layer. Part I: Momentum flux. *J. Atmos. Sci.,* **64,** 1089–1102.

Garman, K. E., and Coauthors, 2006: An airborne and wind tunnel evaluation of a wind turbulence measurement system for aircraft-based flux measurements. *J. Atmos. Oceanic Technol.,* **23,** 1696–1708.

Garratt, J. R., 1977: Review of drag coefficients over oceans and continents. *Mon. Wea. Rev.,* **105,** 915–929.

——, 1992: *The Atmospheric Boundary Layer.* Cambridge University Press, 316 pp.

Geernaert, G. L., 1990: Bulk parameterizations for the wind stress and heat flux. *Surface Waves and Fluxes,* Vol. 1, G. L. Geernaert and W. L. Plant, Eds., Kluwer, 91–172.

Grachev, A. A., and C. W. Fairall, 2001: Upward momentum transfer in the marine boundary layer. *J. Phys. Oceanogr.,* **31,** 1698–1711.

——, ——, J. E. Hare, J. B. Edson, and S. D. Miller, 2003: Wind stress vector over ocean waves. *J. Phys. Oceanogr.,* **33,** 2408–2429.

——, E. L Andreas, C. W. Fairall, P. S. Guest, and P. O. G. Persson, 2007a: SHEBA flux-profile relationships in the stable atmospheric boundary layer. *Bound.-Layer Meteor.,* **124,** 315–333.

——, ——, ——, ——, and ——, 2007b: On the turbulent Prandtl number in the stable atmospheric boundary layer. *Bound.-Layer Meteor.,* **125,** 329–341.

Ingel, L. Kh., 2011: On the effect of spray on the dynamics of the marine atmospheric surface layer in strong winds. *Izv. Atmos. Ocean. Phys.,* **47,** 119–127.

Janssen, J. A. M., 1997: Does wind stress depend on sea-state or not?—A statistical error analysis of HEXMAX data. *Bound.-Layer Meteor.,* **83,** 479–503.

Jarosz, E., D. A. Mitchell, D. W. Wang, and W. J. Teague, 2007: Bottom-up determination of air–sea momentum exchange under a major tropical cyclone. *Science,* **315,** 1707–1709.

Johnson, H. K., J. Højstrup, H. J. Vested, and S. E. Larsen, 1998: On the dependence of sea surface roughness on wind waves. *J. Phys. Oceanogr.,* **28,** 1702–1716.

Jones, I. S. F., and Y. Toba, Eds., 2001: *Wind Stress over the Ocean.* Cambridge University Press, 307 pp.

Khelif, D., S. P. Burns, and C. A. Friehe, 1999: Improved wind measurements on research aircraft. *J. Atmos. Oceanic Technol.,* **16,** 860–875.

——, C. A. Friehe, H. Jonsson, Q. Wang, and K. Rados, 2005: Wintertime boundary-layer structure and air–sea interaction over the Japan/East Sea. *Deep-Sea Res. II,* **52,** 1525–1546.

Kitaigorodskii, S. A., and Yu. A. Volkov, 1965: On the roughness parameter of the sea surface and the calculation of momentum flux in the near-water layer of the atmosphere. *Izv. Atmos. Ocean. Phys.,* **1,** 566–574.

Klipp, C. L., and L. Mahrt, 2004: Flux-gradient relationship, self-correlation and intermittency in the stable boundary layer. *Quart. J. Roy. Meteor. Soc.,* **130,** 2087–2103.

Kraus, E. B., 1968: What we do not know about the sea-surface wind stress. *Bull. Amer. Meteor. Soc.,* **49,** 247–253.

——, and J. A. Businger, 1994: *Atmosphere–Ocean Interaction.* 2nd ed. Oxford University Press, 362 pp.

Kudryavtsev, V. N., 2006: On the effect of sea drops on the atmospheric boundary layer. *J. Geophys. Res.,* **111,** C07020, doi:10.1029/2005JC002970.

Lenschow, D. H., 1986: Aircraft measurements in the boundary layer. *Probing the Atmospheric Boundary Layer,* D. H. Lenschow, Ed., Amer. Meteor. Soc., 39–55.

Lighthill, J., 1999: Ocean spray and the thermodynamics of tropical cyclones. *J. Eng. Math.,* **35,** 11–42.

Mahrt, L., and D. Khelif, 2010: Heat fluxes over weak SST heterogeneity. *J. Geophys. Res.,* **115,** D11103, doi:10.1029/2009JD013161.

——, D. Vickers, P. Frederickson, K. Davidson, and A.-S. Smedman, 2003: Sea-surface aerodynamic roughness. *J. Geophys. Res.,* **108,** 3171, doi:10.1029/2002JC001383.

——, ——, E. L Andreas, and D. Khelif, 2012: Sensible heat flux in near-neutral conditions over the sea. *J. Phys. Oceanogr.,* **42,** 1134–1142.

Makin, V. K., 2005: A note on the drag of the sea surface at hurricane winds. *Bound.-Layer Meteor.,* **115,** 169–176.

Melville, W. K., 1977: Wind stress and roughness length over breaking waves. *J. Phys. Oceanogr.,* **7,** 702–710.

Monin, A. S., and A. M. Yaglom, 1971: *Statistical Fluid Mechanics: Mechanics of Turbulence.* Vol. 1. MIT Press, 769 pp.

Moon, I.-J., T. Hara, I. Ginis, S. E. Belcher, and H. L. Tolman, 2004: Effect of surface waves on air–sea momentum exchange. Part I: Effect of mature and growing seas. *J. Atmos. Sci.,* **61,** 2321–2333.

——, I. Ginis, T. Hara, and B. Thomas, 2007: A physics-based parameterization of air–sea momentum flux at high wind speeds and its impact on hurricane intensity predictions. *Mon. Wea. Rev.,* **135,** 2869–2878.

Mueller, J. A., and F. Veron, 2009: Nonlinear formulation of the bulk surface stress over breaking waves: Feedback mechanisms from air-flow separation. *Bound.-Layer Meteor.,* **130,** 117–134.

Neumann, G., 1956: Wind stress on water surfaces. *Bull. Amer. Meteor. Soc.,* **37,** 211–217.

——, and W. J. Pierson Jr., 1966: *Principles of Physical Oceanography.* Prentice-Hall, 545 pp.

Nicholls, S., and C. J. Readings, 1979: Aircraft observations of the structure of the lower boundary layer over the sea. *Quart. J. Roy. Meteor. Soc.,* **105,** 785–802.

Oost, W. A., G. J. Komen, C. M. J. Jacobs, and C. Van Oort, 2002: New evidence for a relation between wind stress and wave age from measurements during ASGAMAGE. *Bound.-Layer Meteor.,* **103,** 409–438.

Panofsky, H. A., and J. A. Dutton, 1984: *Atmospheric Turbulence: Models and Methods for Engineering Applications.* John Wiley and Sons, 397 pp.

Paulson, C. A., 1970: The mathematical representation of wind speed and temperature profiles in the unstable atmospheric surface layer. *J. Appl. Meteor.,* **9,** 857–861.

Persson, P. O. G., J. E. Hare, C. W. Fairall, and W. D. Otto, 2005: Air-sea interaction processes in warm and cold sectors of extratropical cyclonic storms observed during FASTEX. *Quart. J. Roy. Meteor. Soc.,* **131,** 877–912.

Petersen, G. N., and I. A. Renfrew, 2009: Aircraft-based observations of air–sea fluxes over Denmark Strait and the Irminger Sea during high wind speed conditions. *Quart. J. Roy. Meteor. Soc.,* **135,** 2030–2045.

Powell, M. D., P. J. Vickery, and T. A. Reinhold, 2003: Reduced drag coefficient for high wind speeds in tropical cyclones. *Nature,* **422,** 279–283.

Roll, H. U., 1965: *Physics of the Marine Atmosphere.* Academic Press, 426 pp.

Romero, L., and W. K. Melville, 2010: Airborne observations of fetch-limited waves in the Gulf of Tehuantepec. *J. Phys. Oceanogr.,* **40,** 441–465.

Rutgersson, A., A.-S. Smedman, and U. Högström, 2001: Use of conventional stability parameters during swell. *J. Geophys. Res.,* **106,** 27 117–27 134.

Sanford, T. B., J. F. Price, J. B. Girton, and D. C. Webb, 2007: Highly resolved observations and simulations of the ocean response to a hurricane. *Geophys. Res. Lett.,* **34,** L13604, doi:10.1029/2007GL029679.

Shpund, J., M. Pinsky, and A. Khain, 2011: Microphysical structure of the marine boundary layer under strong wind and spray formation as seen from simulations using a 2D explicit microphysical model. Part I: The impact of large eddies. *J. Atmos. Sci.,* **68,** 2366–2384.

Smedman, A.-S., M. Tjernström, and U. Högström, 1994: The near-neutral marine atmospheric boundary layer with no surface shearing stress: A case study. *J. Atmos. Sci.,* **51,** 3399–3411.

Smith, S. D., 1980: Wind stress and heat flux over the ocean in gale force winds. *J. Phys. Oceanogr.,* **10,** 709–726.

——, 1988: Coefficients for sea surface wind stress, heat flux, and wind profiles as a function of wind speed and temperature. *J. Geophys. Res.,* **93,** 15 467–15 472.

——, and Coauthors, 1992: Sea surface wind stress and drag coefficients: The HEXOS results. *Bound.-Layer Meteor.,* **60,** 109–142.

Soloviev, A., and R. Lukas, 2010: Effects of bubbles and sea spray on air-sea exchange in hurricane conditions. *Bound.-Layer Meteor.,* **136,** 365–376.

Stull, R. B., 1988: *An Introduction to Boundary Layer Meteorology.* Kluwer, 666 pp.

Sun, J., J. F. Howell, S. K. Esbensen, L. Mahrt, C. M. Greb, R. Grossman, and M. A. LeMone, 1996: Scale dependence of air–sea fluxes over the western equatorial Pacific. *J. Atmos. Sci.,* **53,** 2997–3012.

——, D. Vandemark, L. Mahrt, D. Vickers, T. Crawford, and C. Vogel, 2001: Momentum transfer over the coastal zone. *J. Geophys. Res.,* **106,** 12 437–12 448.

Sutton, O. G., 1953: *Micrometeorology.* McGraw-Hill, 333 pp.

Sverdrup, H. U., M. W. Johnson, and R. H. Fleming, 1942: *The Oceans.* Prentice-Hall, 1087 pp.

Toba, Y., S. D. Smith, and N. Ebuchi, 2001: Historical drag expressions. *Wind Stress over the Ocean,* I. S. F. Jones and Y. Toba, Eds., Cambridge University Press, 35–53.

von Arx, W. S., 1967: *An Introduction to Physical Oceanography.* Addison-Wesley, 422 pp.

Wieringa, J., 1993: Representative roughness parameters for homogeneous terrain. *Bound.-Layer Meteor.,* **63,** 323–363.

Wilson, B. W., 1960: Note on surface wind stress over water at low and high wind speeds. *J. Geophys. Res.,* **65,** 3377–3382.

Wu, J., 1969: Wind stress and surface roughness at air-sea interface. *J. Geophys. Res.,* **74,** 444–455.

——, 1980: Wind-stress coefficients over sea surface near neutral conditions—a revisit. *J. Phys. Oceanogr.,* **10,** 727–740.

Wyngaard, J. C., 2010: *Turbulence in the Atmosphere.* Cambridge University Press, 393 pp.

Zhang, J. A., W. M. Drennan, P. G. Black, and J. R. French, 2009: Turbulence structure of the hurricane boundary layer between the outer rainbands. *J. Atmos. Sci.,* **66,** 2455–2467.

Zilitinkevich, S. S., 1969: On the computation of the basic parameters of the interaction between the atmosphere and the ocean. *Tellus,* **21,** 17–24.